*Journal of Applied Fluid Mechanics*, Vol. 18, No. 3, pp. 601-616, 2025.
Available online at www.jafmonline.net, ISSN 1735-3572, EISSN 1735-3645.
https://doi.org/10.47176/jafm.18.3.3003

# Piezoelectric Sensors Placement Strategy for Accurate Acoustic Data Evaluation in Cavitation-induced Erosion Processes

A. Nasseroleslami[1], A. Sarreshtehdari[†1] and M. S. Seif[2]

[1] *Shahrood University of Technology, Shahrood, Semnan, Iran*
[2] *Sharif University of Technology, Tehran, Iran*

†*Corresponding Author Email: sarreshtehdari@shahroodut.ac.ir*

## ABSTRACT

Evaluation of cavitation erosion risk, whether through numerical (CFD) or experimental methods, is crucial in many fluid flow design processes. This risk correlates directly with cavitation signals on affected surfaces. The aim of this study is to optimize the placement of piezoelectric sensors to investigate cavitation-induced erosion on solid surfaces and to enhance the numerical evaluation of their correlation with recorded signals from the sensors. In this study, based on the technical specifications of the K23 tunnel, a convergent-divergent channel has been designed to reduce the pressure in its test section below the vapor pressure, thereby creating the potential for bubble formation on the sample plate. Within this channel, four semi-cylindrical bluff bodies have been utilized as the most effective obstacles to increase cavitation erosion. A quick method for identifying cavitation erosion involves applying a special color to the sample plate. The Film Applicator has been employed as the optimal tool for achieving a uniform color and a thin paint layer on the sample plate. Through CFD modeling, potential cavitation zones are identified under various test conditions to refine the placement of piezoelectric sensors in experimental tests. As a result, piezoelectric sensors are positioned more accurately to measure sound pressure levels. The sound pressure levels obtained using piezoelectric sensors in the time domain, are compared with erosion-induced cavitation zones on the sample test surfaces. The strong agreement between sound pressure levels and observed erosion on the sample plates confirms the accuracy and improvement in the placement of piezoelectric sensors based on CFD modeling.

***Article History***

*Received July 24, 2024*
*Revised October 6, 2024*
*Accepted October 18, 2024*
*Available online January 1, 2025*

***Keywords:***

*Placement of the piezoelectric*
*Erosion*
*Sound pressure level*
*Cavitation tunnel K23*
*Bluff body*

## 1. INTRODUCTION

Cavitation is the formation and collapse of vapor-filled cavities or bubbles in a liquid when it is subjected to rapid pressure changes. This phenomenon occurs when the local pressure drops below the liquid's vapor pressure, leading to vaporization. When the bubbles collapse in higher-pressure areas, they generate shock waves that can cause damage, such as pitting or erosion, to surrounding surfaces. Cavitation erosion in hydraulic machines, such as turbines and pumps, often leads to a significant reduction in the useful life of affected components and has serious implications for maintenance costs and operational efficiency. The primary damage caused by cavitation is erosion, which can range from mild surface wear to severe material loss, adversely affecting the performance of fluid-related machinery and potentially leading to operational disruptions or catastrophic failures. There are various methods for detecting cavitation, with one of the quickest and most cost-effective approaches being the use of piezoelectric sensors to capture acoustic signals generated by cavitation. Analyzing the relationship between acoustic signals and the extent of erosion can facilitate the accurate assessment of erosion levels. Next, this study first examines research related to the selection of semi-cylindrical bluff bodies, followed by an investigation into methods of cavitation generation and the detection of erosion resulting from cavitation.

Yamagata et al. (2016) studied the sound generated by flow over objects placed in a uniform flow at various angles of attack from a semi-circular cylinder and compared the results with those from circular cylinder. The results indicate that when flow encounters the smooth surface of semi-circular cylinders, it can significantly increase flow erosion. In an experimental study, Escaler et al. installed semi-circular obstacles on the suction side of a hydrofoil to modify the flow field and alter the erosion

rate. They tested four different obstacles and found that a semi-circular cross-section is the most suitable geometry for producing repeatable cavities on samples in a short period (Escaler et al., 2001). Another study by the same group observed that such obstacles cause severe localized erosion due to the collapse of strong cavitation vortices in a narrow region (Escaler et al., 2003). Furthermore, previous studies at Andritz Hydro have shown that flow behind a semi-circular cylinder can be entirely erosive, and the erosion pattern varies with changes in flow velocity and the inclusion or removal of the cylinder (Ghahramani et al., 2020). Based on these works, Queiroz et al. focused on studying different cavitation regimes behind a semi-circular cylinder to understand the various flow characteristics around sharp-edged bluff bodies.

In very few articles that have addressed the relationship between noise generated by cavitation bubble collapse and cavitation erosion, there is no precise pattern or relationship established between noise and erosion that could predict or model erosion. For example, Varga et al. compared erosion intensity and noise levels by conducting experiments on a cylindrical cylinder in a cavitation tunnel and stated that maximum cavitation erosion intensity occurs at the point of maximum noise level (Varga et al., 1969). However, a detailed pattern and relationship between noise level and erosion rate have not been presented. Jahangir et al. (2021) utilized a method involving painted surfaces to reduce testing time in the cavitation examination, but even with this method, drying the paint requires 24 hours. Therefore, the methods used for identifying cavitation erosion will be very time-consuming. Ylönen et al. (2020) examined cavitation erosion of polished stainless steel cylindrical samples in a high-speed cavitation tunnel. The cavities created in the samples were measured using an optical profilometer, and cavitation damage was characterized by the distribution of cavity diameters. They concluded that acoustic emission (AE) analysis can be used for monitoring cavity formation without visually inspecting the damaged surface, providing a basis for potential future applications in non-intrusive monitoring of cavitation erosion in hydraulic machinery. Flageul et al. (2012) proposed a method for predicting cavitation damage using cavitation flow simulations. However, a significant discrepancy was found between simulated and experimental results for unstable upstream cavitation flows, indicating that Computational Fluid Dynamics (CFD) tools need improvement for better simulation in this area. Hattori & Ishikura, (2010) revisited the cavitation erosion database and analyzed data from stainless steel, defining erosion resistance as a reciprocal erosion rate. They found that the correlation between erosion resistance and sample hardness after erosion testing was better than that of other mechanical properties, providing a reliable estimation of cavitation erosion resistance in different stainless steels. Richman & Mcnaughton, (1990) concluded from experiments conducted with a vibration device that there is a good correlation between material removal rate and cyclic deformation parameters, indicating that fatigue damage is a predominant process in cavitation erosion. The dominant feature in cavitation erosion resistance is the fatigue strength coefficient $\sigma f'$, which forms the greatest difference between materials. Zhang et al., (2022) developed a numerical estimation approach for cavitation erosion and extracted various hydrodynamic cavitation mechanisms. They simulated large eddies to estimate the cavitation erosion region energetically, providing a foundation for future studies on cavitation erosion mechanisms. Garcia & Hammitt, (1966) compiled a comprehensive dataset of cavitation damage in a vibration facility using water, mercury, lithium, and lead-bismuth alloys as test fluids and covering various temperature coatings from room temperature to 1500 degrees Fahrenheit. They derived a simple and relatively accurate equation to predict derived damage, showing that ultimate flexibility is largely the most effective material property for predicting cavitation damage. Karimi & Martin, (2013) evaluated erosion and material reaction regarding the stress field generated by cavitation collapse and subsequent physical and chemical processes aiding erosion damages. This work describes experimental methods for assessing erosion damage, followed by presenting erosion damage results from various laboratory apparatuses. Momma & Lichtarowicz, (1995) used polyvinylidene fluoride (PVDF) piezoelectric polymer to measure and count pressure pulses generated by cavitation in a cavitation jet device. The mass loss of aluminum specimens in the test correlated with pressure pulse data. Steller et al., (2015) compared experimental cavitation erosion data across a group of materials obtained from 15 different laboratories. Among the equipment used for these experiments, the most significant differences in terms of mass loss or penetration depth can be observed in cavitation tunnels and rotating disk facilities.

Various methods have been proposed and developed so far for detecting cavitation erosion. Four common types of methods used for detecting cavitation erosion are: A) Colorimetric test methods. These methods dye the parts relevant to the target sample and estimate cavitation erosion by observing color removal. Although a few studies have been conducted using this method (Ghahramani et al., 2020; Ju & Choi, 2022; Jahangir et al., 2021), cavitation erosion is directly detected with this method, yielding very accurate results. However, due to issues in selecting suitable colors and the time-consuming nature, online detection is complex and challenging. B) Acoustic noise measurement methods for cavitation. These methods use audible sound (Čudina & Prezelj, 2008; Čudina, 2003), cavitation noise (Bajic, 2002; Varga et al., 1969; Ge et al., 2016), and other sources as indirect detection methods for cavitation erosion. However, the correlation between cavitation and cavitation erosion is complex, as they do not always have a positive relationship, making it difficult to use these methods for accurately estimating the status of cavitation erosion. C) Vibration test methods. These methods (Varga et al., 1969; François, 2012; Hattori et al., 1998) are also indirect detection methods that estimate the condition of cavitation erosion by examining the vibration status of fluid-related machinery. However, the components forming the vibration signals are very complex and Separating the vibration component related to cavitation erosion from the collected vibration signals is very challenging. D) Acoustic Emission (AE) is a phenomenon involving the

release of transient stress waves. One of its applications is detecting certain types of failures, such as plastic deformation, cracking, and similar events, in a localized area of the material. AE has been considered a primary candidate for non-destructive testing (NDT) of material flaws or structural damages for many years and has found wide applications in these fields (Elforjani & Mba, 2009; Jirarungsatian & Prateepasen, 2010). He & Shen, (2022) proposed a direct detection method for cavitation erosion using AE techniques. Based on the material damage mechanism in the cavitation erosion process, assumptions regarding the AE characteristics of cavitation erosion are proposed and qualitatively confirmed by experiments. The method used in this experiment is a specific approach that can combine the first and second methods (although piezoelectric sensors have rarely been used in the second method until now). In fact, color is used to quickly identify the cavitation erosion threshold, while piezoelectric sensors are employed to record signals. The signals recorded from the start of the experiment to the cavitation erosion threshold can be useful in evaluating the proper arrangement of piezoelectric sensors and in researching the relationship between acoustic waves generated by cavitation and the surface erosion threshold.

Lush & Angell, (1984) investigated the correlation between the cavitation erosion rate of 99% pure aluminum and the acoustic pressure level of cavitation noise. Logarithmic regression analysis of the cavitation erosion rate at the sound pressure level expressed in decibels indicates a significant correlation for each configuration, independent of fluid velocity and cavitation number, although there is a very large probable error. De & Hammitt, (1982) examined the correlation between cavitation noise and damage, its source, and variance with flow parameters. Cavitation pressure pulses were monitored by measuring peak pulse amplitudes in a cavitation venturi. The derived acoustic power from the pulse height spectrum (PHS) varies with the nth power of the venturi throat velocity, where $6.8 < n < 10.5$. It has also been acknowledged that for more accurate prediction of cavitation erosion extent, more PHS measurements are needed to obtain precise information regarding the amplitude and frequency characteristics of pressure pulses under different flow conditions.

In this research, a converging-diverging channel was designed and fabricated to achieve high velocity in the test section. Additionally, a semi-cylindrical body was installed as the optimal bluff body to induce cavitation in the test section. The most efficient and fastest method identified for accelerating the cavitation process involves using a specific color on the sample plate. After conducting various experiments, it was determined that the use of a Film Applicator is suitable for creating uniform color and thin thickness, contrary to the claim by Jahangir et al., 2021, injecting ink with a syringe creates a thickness close to 1 mm. In this study, for the first time, an optimal arrangement of piezoelectric sensors was used to record signals generated by the cavitation process using CFD analysis, and the comparison of signals recorded by piezoelectric sensors and the erosion created on the sample plate demonstrates the correct functioning of the piezoelectric sensors.

## 2. EXPERIMENTAL SETUP

In this experiment, using the cavitation-induced acoustics strategy, erosion can be detected by observing the generated acoustic pattern, without the need for several days of testing. To create suitable conditions for conducting the experiment and inducing cavitation, a converging-diverging nozzle is used at the measurement section.

Initially, the pressure needs to be reduced below the vapor pressure of water to create conditions for bubble formation. Subsequently, by increasing the pressure and collapsing the bubbles, erosion can be induced in the specimen placed in the test section. In this experiment, a special ink was used to apply color onto the sample plate. Various methods were employed, including injecting ink with a syringe and spraying ink using different spray methods, for cavitation erosion testing, but these were not successful. Spraying ink with different spray methods increases the adhesion of the ink to the sample plate, while using a syringe results in thicker layers of ink, which complicate the detection of cavitation erosion. The best method for achieving uniform color with minimal thickness on the sample plate, to prevent excessive adhesion of the ink, is using a Film Applicator. This component is marked with four dimensions: 30, 60, 90, and 120 micrometers. The face with the required dimension is placed on the sample plate. Subsequently, the special ink is poured into the designated area, and then drawn uniformly from top to bottom across the sample plate. In Fig. 1, the use of this device to achieve an ink thickness of 30 μm is demonstrated. Another method was also employed to measure ink thickness. A portion of the sample plate was prepared using cold mounting, and the thickness of the ink was checked using an optical microscope, as shown in Fig. 2.

The schematic diagram of the designed equipment for use in the measurement section of cavitation tunnel K23 is shown in Fig. 3. According to the explanations provided in the introduction and the studies conducted by (Escaler et al., 2001; Escaler et al., 2003; Ghahramani et al., 2020), the use of a semi-cylindrical cylinder is the most suitable geometry for generating repeatable cavities on the specimen in a short period of time. This geometry can effectively accelerate the erosion process.

Based on this premise, in this experiment, a semi-cylindrical cylinder has also been used to enhance the erosion process. At the inlet of the flow onto the specimen plate, a semi-cylindrical bluff body is used. The bluff body increases and channels the erosion caused by cavitation on the specimen plate compared to cases without a bluff body. Consequently, when a bluff body is present, less force is required in the system to induce erosion. Initially, it is necessary to determine the minimum inlet velocity to the test section required for cavitation to form. Additionally, the distance downstream from the bluff body where cavitation can form should be identified.

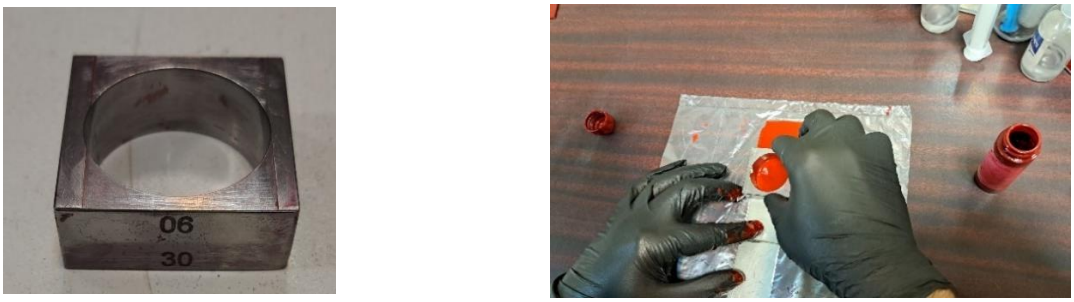


(a) (b)

**Fig. 1 (a) Film Applicator (b) Application of color onto the sample plate using a Film Applicator**

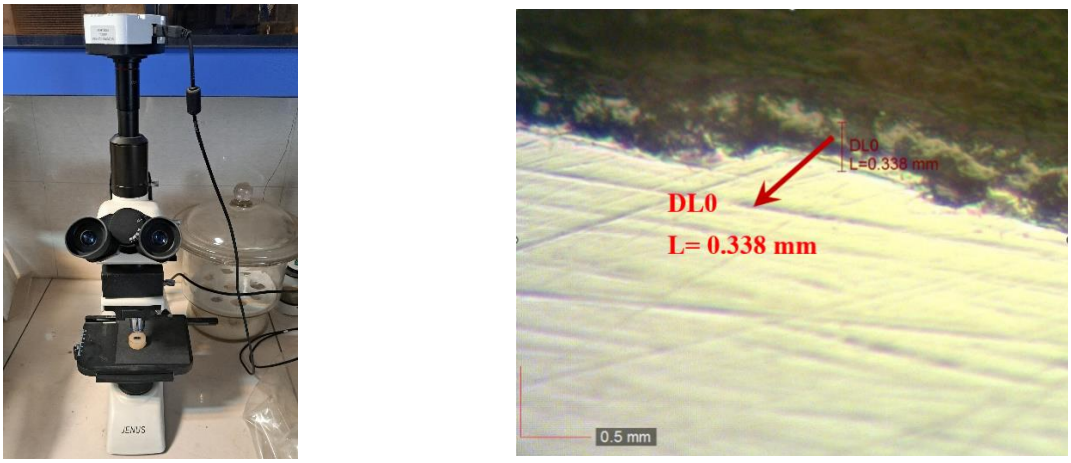


(a) (b)

**Fig. 2 (a) Measurement of ink thickness on the sample plate (prepared using the Cold mounting method) using the JENUS optical microscope (b) Ink thickness of 0.338 mm reported by the microscope**

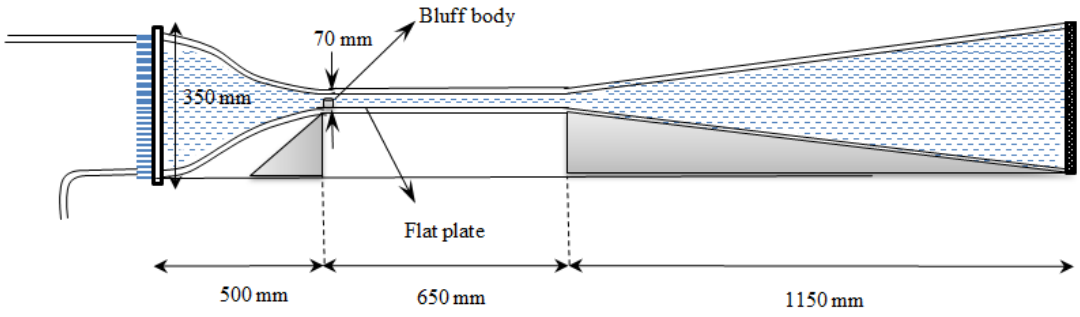


(a)

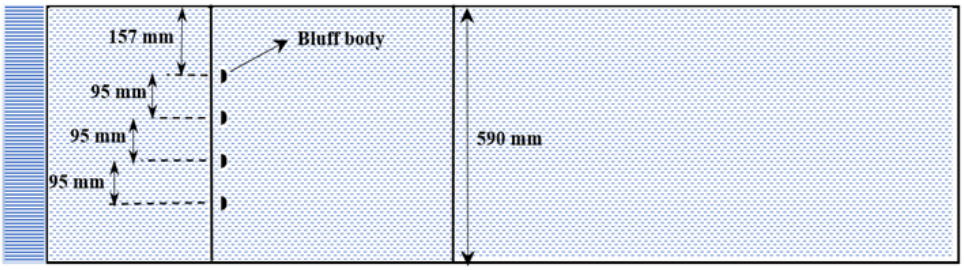


(b)

**Fig. 3 (a) Side view schematic of the designed equipment for use in the test section of cavitation tunnel K23 (b) Top view schematic of the designed equipment for use in the test section of cavitation tunnel K23**

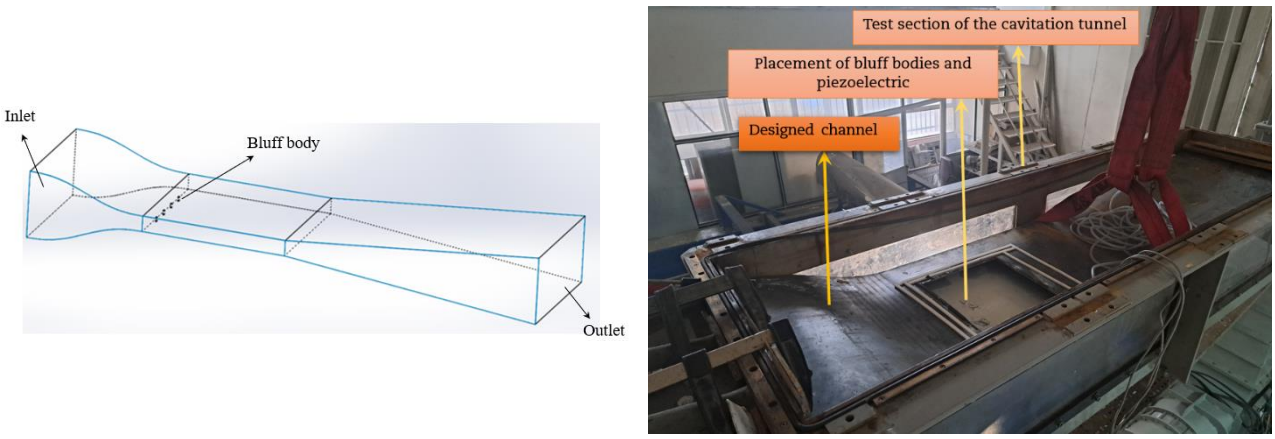


(a) (b)

**Fig. 4 (a) Schematic of the designed equipment for installation in the measurement section (b) Installation of the designed channel in the test section of the cavitation tunnel**

Computational Fluid Dynamics (CFD) analysis is used to address these questions, to specify the size of the specimen plate after the bluff body, and to define the arrangement of the piezoelectric sensors.

### 2.1 Hydrodynamic Analysis of the Measurement Section Using Computational Fluid Dynamics (CFD)

Based on the explanations provided in the introduction, a painted sample plate placed downstream of a bluff body is used to investigate the relationship between acoustic information resulting from cavitation stored by piezoelectric devices and the eroded sample plate. However, what should be the dimensions of the sample plate? How should the piezoelectric sensors be arranged? And what should be the minimum inlet water velocity into the test section to induce cavitation? Flow simulation has been conducted to answer these questions. This simulation was performed using the Star CCM+ software at inlet velocities ranging from 2.5 m/s to 3.5 m/s into the test section.

Among the important equations governing fluid dynamics that are widely used in solving fluid problems, we can mention the continuity equation and the Navier-Stokes equations, which are presented as Eq. (1) and Eq. (2).

$$\frac{\partial \rho}{\partial t}+\frac{\partial}{\partial x_i}\left(\rho u_i\right)=0 \tag{1}$$

(2)

In the equations above, $x$، $u$، $\mu$، $\rho$ and p represent, respectively, position, velocity, viscosity, density, and pressure. The subscripts $i$ and $j$ count the three axes x, y, and z. The term $\left(-\overline{\rho u_i' u_j'}\right)$ in Eq. (2) is known as Reynolds stress and can be computed using turbulence models (Nadery et al., 2021). In this problem, the Schnerr-Sauer model is employed, which represents the changes in density due to bubble formation and cavitation by using a mixture density approach. This approach takes into account the volume fraction of vapor as well as the densities of both the liquid and vapor phases. This model captures the significant variations in density that occur as bubbles form, grow, and collapse during cavitation.

In Fig. 3 and Fig. 4, the geometry of the designed equipment in SolidWorks for simulating the problem is depicted. In this simulation, all surfaces except for the inlet and outlet are considered as walls.

According to document K23 Manual (Tunnel, 2001), the maximum inlet velocity into the test section is 3.6 m/s. Therefore, inlet velocities ranging from 2 m/s to 3.5 m/s have been considered for the test section. The boundary condition at the outlet is set to pressure, and its value corresponds to the operational pressure conditions of the flow, which, based on preliminary tests, are close to atmospheric pressure (Relative pressure = 0 atm). Considering the no-slip condition on the tunnel geometries and the bluff body, wall boundary conditions have been applied to these geometries. Table 1 reports the physical models used for the accurate simulation of this problem, as well as the values for the initial conditions.

Furthermore, it should be noted that among the three models of Full Rayleigh–Plesset, Schnerr-Sauer, and Homogeneous Relaxation provided by Star CCM+ software for cavitation modeling, the Schnerr-Sauer model has been used to model the cavitation phenomenon. According to the software guide, the Homogeneous Relaxation model is primarily used for detecting the vapor phase (cavitation) during instantaneous boiling caused by sudden pressure changes (Siemens Digital Industries Software, 2021). Additionally, the Schnerr-Sauer model, derived primarily from simplifying the Full Rayleigh–Plesset model, has been extensively utilized by researchers for cavitation modeling, offering high accuracy in simulating this phenomenon (Sikirica et al., 2019; Lee et al., 2021). In this study, domain meshing was performed using the commercial software Star CCM+, which is capable of creating various types of meshes. The meshing

**Table 1 The selected physics for solving the problem and the initial conditions**

| Selected Physics | Explanations and Reasons | Initial condition parameters | Values used |
|---|---|---|---|
| Three Dimensional | Three-Dimensional Nature of Flow | Pressure | 101000 (pa) |
| Implicit Unsteady | Flow Transient | Turbulence Specification | Intensity + Viscosity Ratio |
| Turbulent | Considering Flow Turbulence | Turbulence Intensity | 0.01 |
| RANS | Computational Efficiency - Achieving Adequate and Desired Accuracy in Cavitation Simulation (Sipilä et al., 2014; Helal et al., 2018; Sikirica et al., 2019) | Turbulent Viscosity Ratio | 10 |
| Realisable K Epsilon Two Layer | Superiority of this Turbulence Model Compared to Other RANS Models (Sikirica et al., 2019) | Inlet velocity to the test section | [3.5 m/s (Water), 0 (Vapor)] |
| Segregated Flow Model | Better Convergence - Desired Accuracy - Increased Computational Speed | Volume Fraction | [1.0 (Water), 0.0 (Vapor)] |
| Two-Layer All y+ Wall Treatment | Using Wall Functions to Improve Simulation Accuracy. y+ size= 1.3, Mesh Base Size= 0.01 m, Relative Minimum Size= 0.0025 m, Minimum Proximity=0.05, Number of Prism Layers= 10, Absolute Size of Prism Layers = 0.001 m, Volumetric Controls: 1- Very Close Proximity to the Bluff Body: Absolute Size= 4.0E-4 m 2- Region Near the Bluff Body: Absolute Size= 0.001 m | Density of Water | 997.56 Kg/m^3 |
| Multiphase | Considering the Multiphase Nature of the Problem | Density of Vapor | 0.595 Kg/m^3 |
| Multiphase Interaction | Interaction of Phases in the Problem and Cavitation Modeling VOF-VOF-Phase Interaction Model: Definition of the primary phase (water) and secondary phase (vapor) in this model (Dunlop, 2015; Siemens Digital Industries Software, 2021) , Schnerr-Sauer Model: This model disregards effects that are not essential for practical applications, making it more suitable for practical use (Brennen, 1995; Siemens Digital Industries Software, 2021) | | |
| Gravity | Due to the Influence of Gravity on the Flow | | |

utilized three models: Surface Remesher, Trimmed Mesher, and Prism Layer Mesher. A representation of the generated mesh is depicted in Fig. 5. To investigate mesh independence, a point downstream of the bluff body, located in a region with potential for vapor volume fraction formation, was selected. The position of this point is shown in Fig. 6. By varying the mesh size across six stages, the pressure at this point was analyzed. As illustrated in Fig. 7, a mesh consisting of 8 million cells was selected for the simulation, as increasing the number of cells beyond this value did not result in any significant change in the pressure at the selected point.

To validate the results obtained from simulating gravity-driven flow in the measurement cross-section, a numerical simulation of the flow in two chambers connected to each other by a channel has been performed. This simulation was compared with the results from the tutorial Star CCM+ (Siemens Digital Industries Software, 2021). In this problem, as shown in Fig. 8, the left chamber is initially filled with water, which flows through the channel into the right chamber. All boundaries are solid walls, except for the upper horizontal surface on the left side, where a constant static pressure (atmospheric) is applied.

Under the influence of gravity, water flows into the right chamber. Simultaneously, water also flows through the upper left boundary to maintain the fluid surface level. The pressure in the right chamber increases due to the compression of air. After some time, all fluid elements

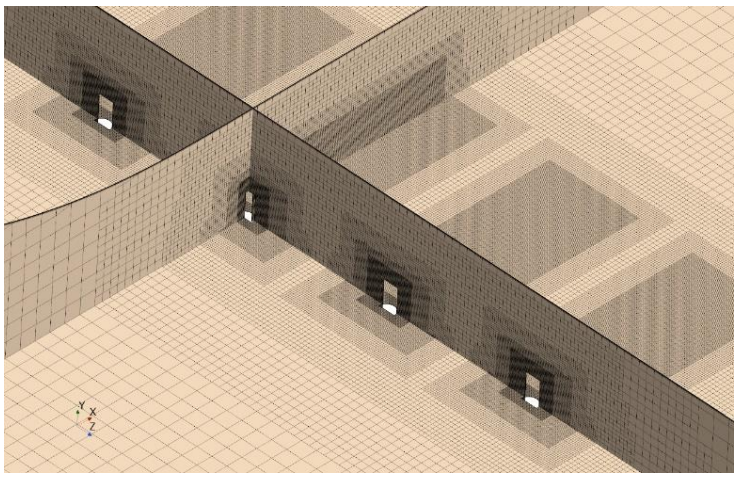

**Fig. 5 Mesh created at the intersection of flat surfaces with a semi-cylindrical shape**

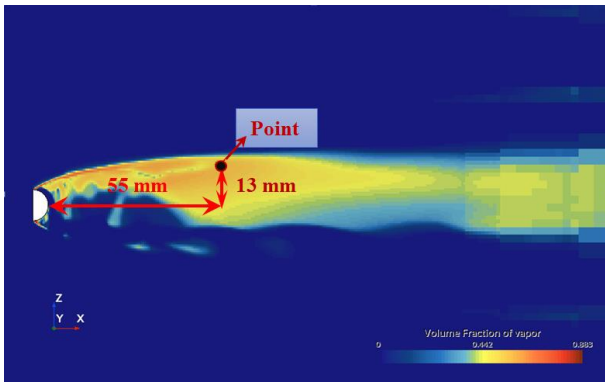


**Fig. 6 Location of a point downstream of the bluff body for the mesh independence study**

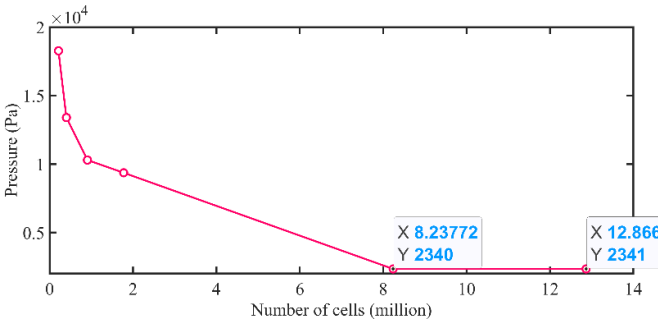


**Fig. 7 Mesh Independence Study**

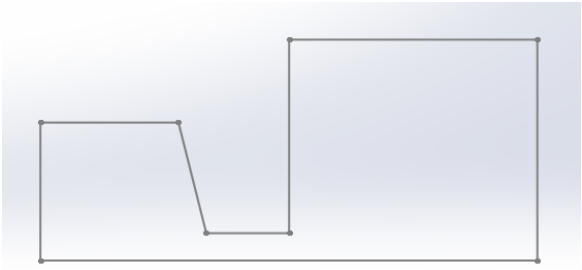

**Fig. 8 Two chambers connected to each other via a channel**

reach a state of rest and hydrostatic equilibrium. This problem involves multiphase flow (two phases of water and air) and turbulent water flow, utilizing the K-Epsilon turbulence model. Gravity acts in the -y direction. The simulation time considered is 5 seconds, and in Fig. 9, the water volume fraction is presented for numerical analysis at 5 seconds. For comparison purposes, the water volume fraction at 5 seconds from the tutorial is also shown in Fig. 9, indicating good agreement with the numerical analysis. Additionally, the pressure generated based on the numerical analysis (Fig. 10 (a)) and the solution provided in the tutorial (Fig. 10 (b)) have been compared, demonstrating strong alignment between them.

## 3. RESULT

### 3.1 The Result of CFD and the Optimal Placement of the Piezoelectric Sensor

As mentioned, simulations were conducted at inlet velocities of 2 m/s, 2.5 m/s, 3 m/s, and 3.5 m/s. Based on the simulation results, the minimum inlet velocity at the test section required to induce cavitation is 2.5 m/s. In Fig. 11, the vapor volume fraction created at velocities of 2 m/s and 2.5 m/s is shown at 1 second, where the vapor volume fraction is not observed at 2 m/s.

The maximum inlet velocity at the test section is 3.5 m/s, which demonstrates an effective vapor volume fraction over a length of 10 cm at this velocity, as shown Fig. 12.

Therefore, a sample plate of 12 cm in length is considered, where 2 cm at the end is designated for attaching the plate to the channel body with a screw. However, it is not feasible to connect the piezoelectric sensor to the sample plate for recording acoustic cavitation data. Attaching the piezoelectric sensor to the plate

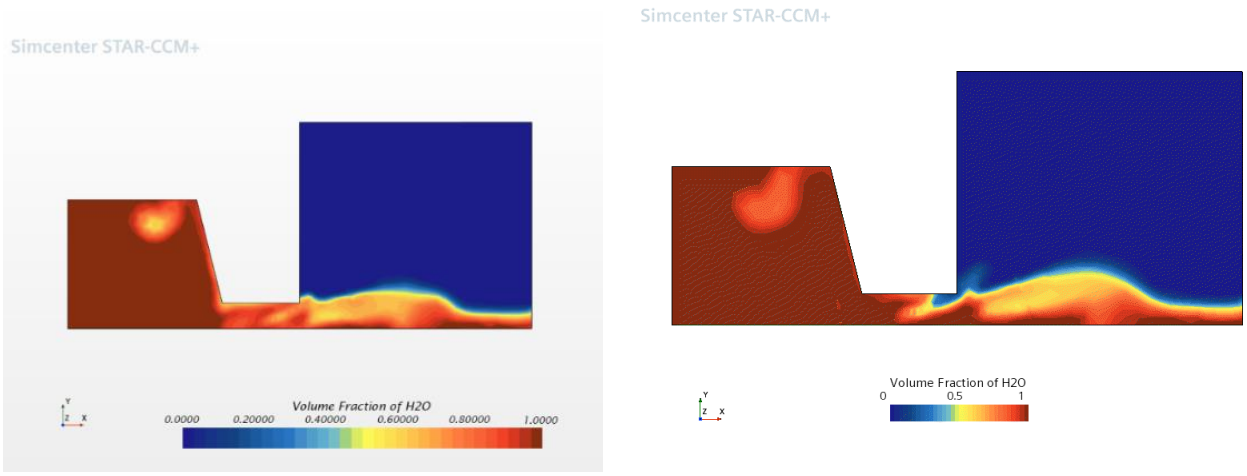


(a) (b)

**Fig. 9 (a): Volume fraction of water by numerical analysis at 5 seconds; (b) Volume fraction of water by the solution performed in the tutorial at 5**

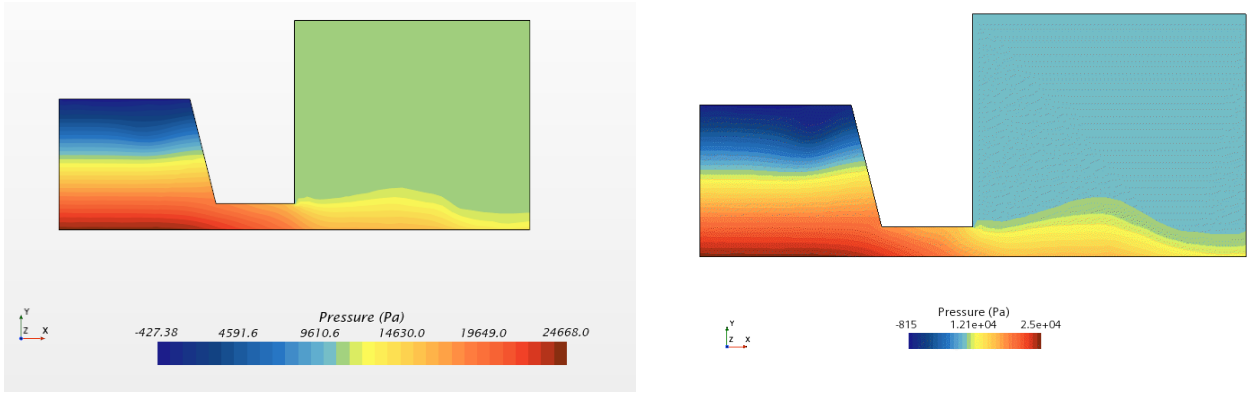


(a) (b)

**Fig. 10 (a): Pressure generated by numerical analysis at 5 seconds; (b) Pressure generated by the solution performed in the tutorial at 5 seconds**

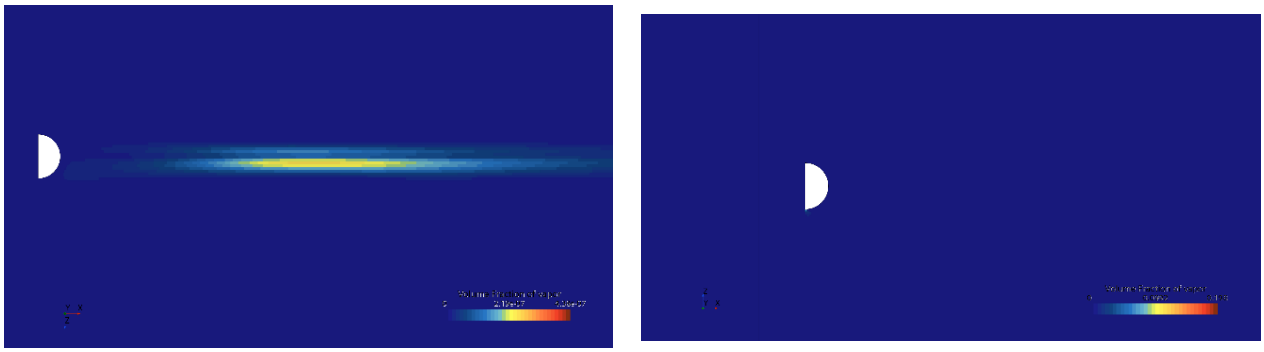

(b) (a)

**Fig. 11 (a) Top view of the vapor volume fraction created at 2 m/s at 1 second; (b) Top view of the vapor volume fraction created at 2.5 m/s at 1 second**

occupies surface area on the sample plate, which results in inaccuracies in calculating the surface erosion area and complicates channel sealing. Because after each test, the sample plate is detached for reinjecting color and calculating the eroded surface area from the channel, the sealing of the section where the piezo wires exit the channel is compromised. If the piezo is connected underneath the sample plate to the channel, the acoustic cavitation signal is not properly transferred to the piezoelectric sensor. This is because the sample plate is attached to the channel using double-sided adhesive and screws, and the pressure generated due to bubble collapse

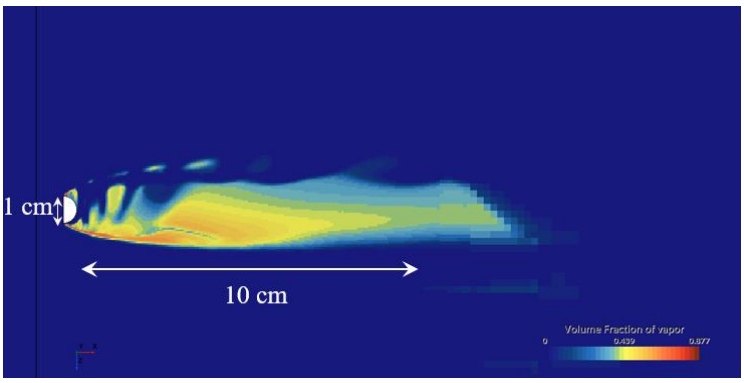


**Fig. 12 Top view of the vapor volume fraction created at a velocity of 3.5 m/s at 1 second**

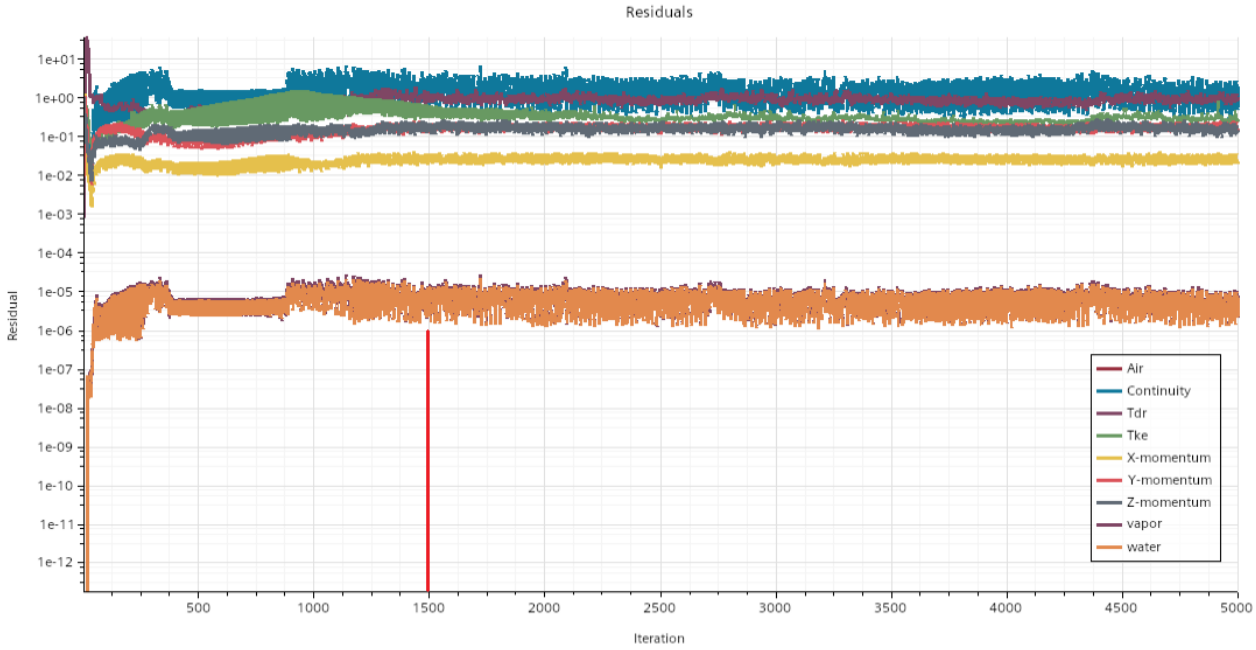


**Fig. 13 The residual of the CFD equations solved at an inlet velocity of 3.5 m/s**

is weakened as it passes through the adhesive and sample plate, before reaching the piezoelectric sensor (Mardin et al., 2023). Therefore, in this scenario, the best solution for connecting the piezoelectric sensor is to install it in a location where the flow pattern and cavitation formation are similar to those behind the main bluff body. Furthermore, according to Fig. 12, three piezoelectric sensors with a diameter of 27 mm each should be used to cover the cavitation region. The creation of the vapor phase is time-dependent, and the numerical analysis conducted is transient. The interval of volume fraction oscillations in vapor creation remains constant after a specific amount of numerical solution, which can be confirmed based on the residual solution of the vapor volume fraction equation. For example, in Fig. 13 residual values from the numerical solution can be observed at an inlet velocity of 3.5 m/s, computed at 1 second. In this instance, after 0.3 seconds, the residual value of the vapor volume fraction equation stabilizes between 1e-5 and 1e-6. This issue has been investigated across all velocities, and it was ultimately determined that after 0.5 seconds, the oscillation range of the vapor volume fraction stabilizes. Therefore, a reliable solution time of 1 second has been considered.

It should be noted that in this problem, three piezoelectrics are not aligned along a single axis, because inevitable surface irregularities due to the connection and waterproofing of the piezoelectric sensors may alter the flow pattern after each of them. Furthermore, according to the conducted CFD analysis, the potential for cavitation inception occurs up to 10 cm after the bluff body, and placing three piezoelectric sensors without spacing is not feasible. For this reason, three additional Bluff Bodies are used, which are placed at a distance from the main Bluff Body. However, to determine their placement, CFD analysis must be used to ensure that the region of pressure changes created behind the Bluff Body does not interfere with one another.

Based on CFD analysis, it has been determined that if the distance between the bluff bodies is 95 mm, the region of pressure and velocity changes behind them does not

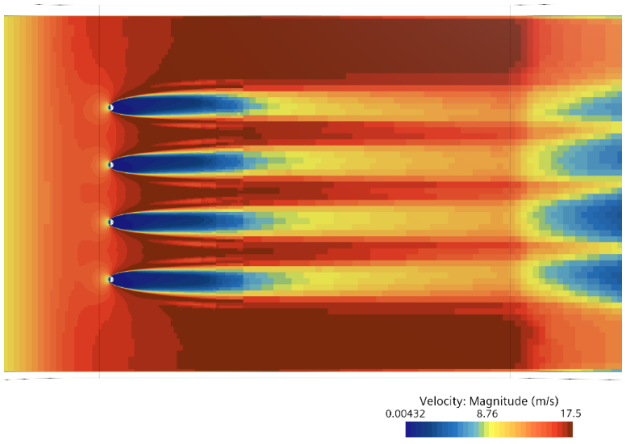


**Fig. 14 Top view of the velocity at an inlet velocity of 3.5 m/s after 1 second**

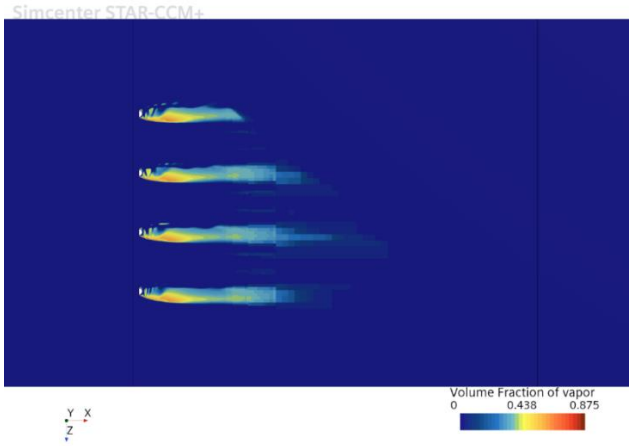


**Fig. 15 Top view of the vapor volume fraction created at a velocity of 3.5 m/s within 1 second**

interfere with each other at all velocities. For example, the velocity contour is shown in Fig. 14. Also, according to Fig. 15, the volume fraction of vapor created after the bluff body is similar to each other.

The volume fraction of vapor created after the bluff body, as shown in Fig. 12 is 10 cm in length and 4 cm in width. Based on CFD analysis, the arrangement of piezoelectric sensors should cover 10 cm longitudinally and 4 cm transversely after the bluff body. The schematic layout of the arrangement of piezoelectric sensors and bluff bodies according to CFD analysis is shown in Fig. 16. In Fig. 17, the volume fraction of vapor generated after the bluff bodies is shown along the x-axis and in the xy plane. Fig. 18 displays the volume fraction of vapor in the yz plane, 11 cm from the bluff body. As shown, the vapor volume in this region is diminished and can be considered negligible. Fig. 19 illustrates the volume fraction of vapor in the yz plane passing through the centers of the piezoelectrics, while Fig. 19 (d) presents these planes simultaneously. The piezoelectrics are labeled according to their distance from the bluff bodies as Piezoelectric 1 (closest distance), Piezoelectric 2, and Piezoelectric 3. In Figures 15 to 17, which are shown in the yz plane, it is observed that the volume fraction of vapor after the four bluff bodies is similar across the figures. The volume

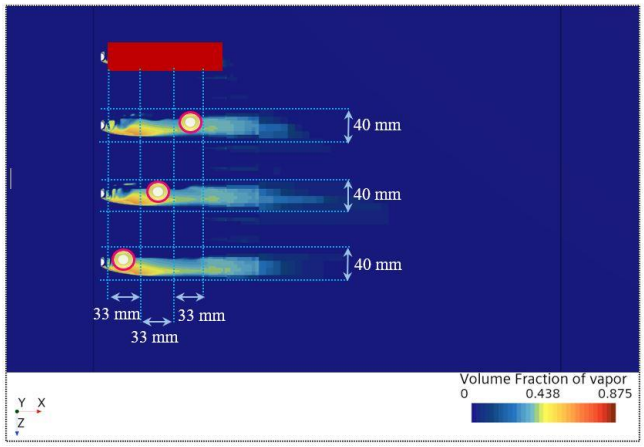


**Fig. 16 The schematic of the piezoelectric placement based on CFD analysis**

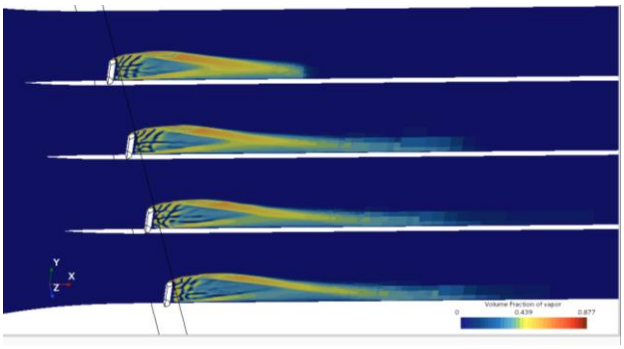

**Fig. 17 Volume fraction of vapor generated after bluff bodies along the x-axis , at a velocity of 3.5 m/s and after 1 second**

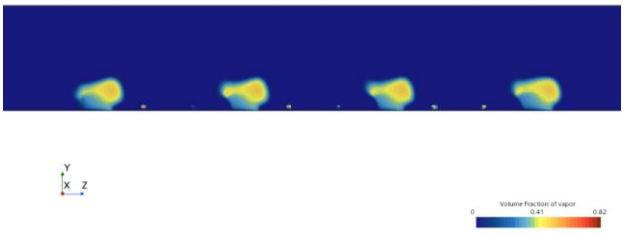

**Fig. 18 Volume fraction of vapor generated in the yz plane at a distance of 11 cm from the bluff body, at a velocity of 3.5 m/s and after 1 second**

fraction of vapor in the planes passing through sensors 1 and 2 is quite similar but larger compared to the plane passing through sensor 3. Furthermore, the practical arrangement of piezoelectric sensors and the sample plate on the channel based on the CFD analysis is depicted in Fig. 20. Fig. 21 shows the dimensions of the sample plate, as well as the distances between the piezoelectric components and the bluff bodies.. The distances between the bluff bodies are configured so that their wake patterns do not interfere with each other. The arrangement of the piezoelectric components is designed to cover the effective vapor volume (10 cm) on the sample plate.

Cavitation signals have been recorded using the GL820 data logger (Fig. 22). The data sampling rate is 100

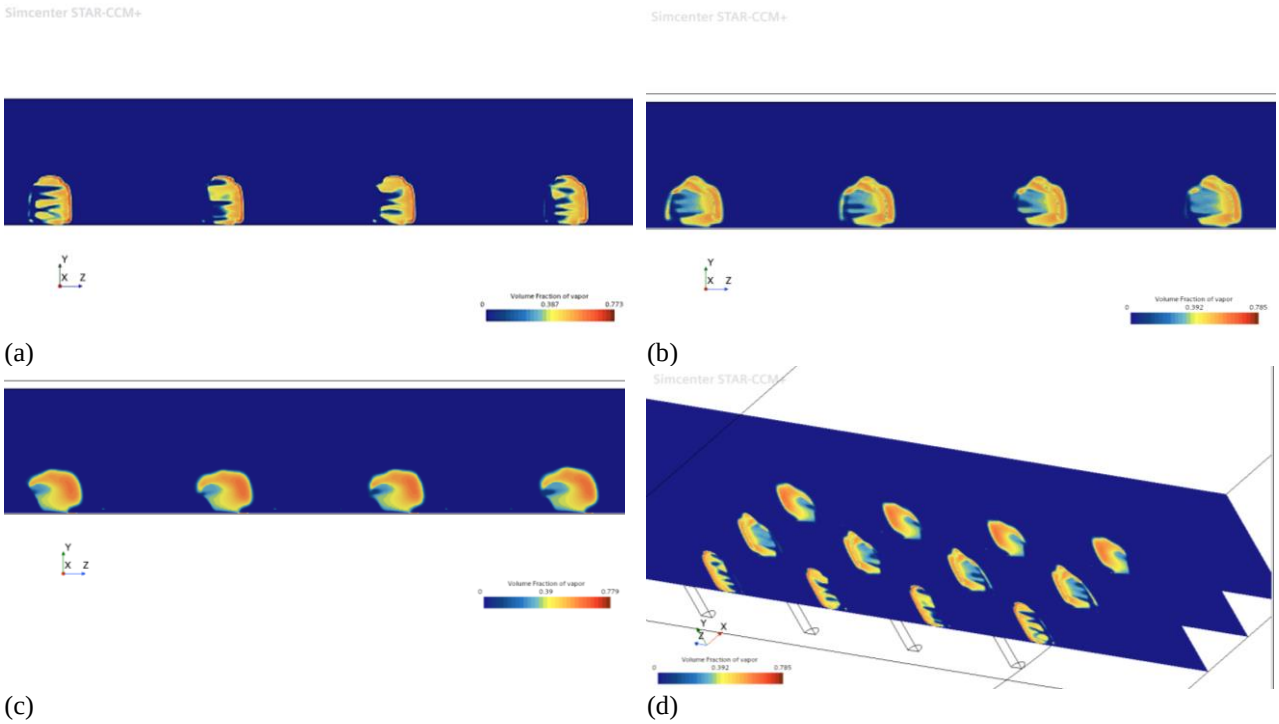


**Fig. 19 Volume fraction of vapor generated in the yz plane passing through the center of the piezoelectric sensors, at a velocity of 3.5 m/s and after 1 second: (a) Plane passing through piezoelectric 1; (b) Plane passing through piezoelectric 2; (c) Plane passing through piezoelectric 3; (d) Planes passing through the piezoelectric sensors simultaneously**

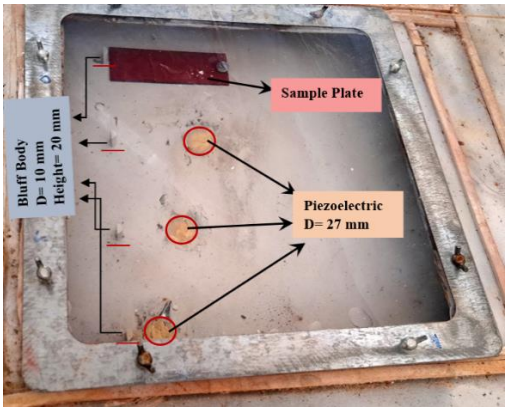


**Fig. 20 Arrangement of piezoelectric sensors and sample plate on the channel based on CFD analysis**

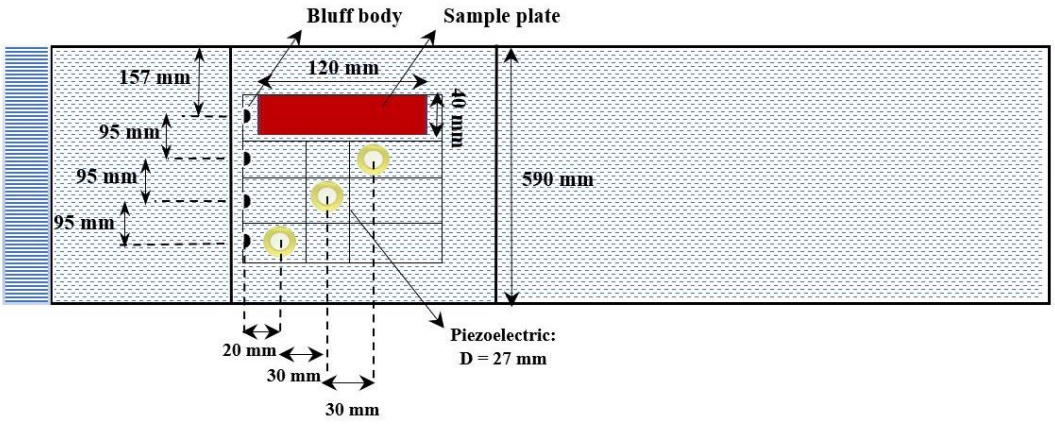


**Fig. 21 Top view schematic of the layout of piezoelectric sensors in the designed equipment for deployment in the test section of cavitation tunnel K23**


**Fig. 22 Connection of piezoelectric sensors and earth wire to the GL820 data logger**

ms or 0.1 Hz. The voltage variation range does not exceed ±1 volt.

### 3.2 Comparison of the Worn Surface Area and the Recorded Signals from the Piezoelectric Sensors

The experiment was conducted at input velocities of 2.5 m/s, 3 m/s, and 3.5 m/s, with test durations of 40 minutes, 50 minutes, 60 minutes, and 70 minutes for each velocity. Based on Fig. 21 and Fig. 25, the sample plate is divided into three sections: A1, A2, and A3. A total of 36 series of signals were obtained. After each experiment, the sample plate is removed from the channel, and an image is captured to examine the level of erosion. To enhance the clarity of the observed erosion in each image, a specific level of illumination (300 lux, due to the medium-light conditions of the space) is applied, and its threshold is recorded in ImageJ software. ImageJ is a powerful, Java-based image processing program widely used for scientific and medical image analysis. ImageJ offers a range of tools for basic and advanced image processing, including filtering, thresholding, and quantitative analysis.

Also, the signals stored from the data logger are converted to pressure using Eq. (3) (COMSOL Simulation of the Direct Piezoelectric Effect, n.d.).

Since piezoelectric signal recording exhibits dynamic behavior, converting voltage signals to pressure using calibration methods designed for static sensors, such as strain gauges or load cells, is not feasible. For example, a common calibration method for static sensors involves applying known weights to the sensor and deriving the relationship between the signal (in volts) and pressure, force, or strain. This method is not applicable to piezoelectric sensors. Therefore, pressure is determined based on relationships derived from the properties and type of the piezoelectric material (COMSOL Simulation of the Direct Piezoelectric Effect, n.d.). In this study, a 27 mm diameter piezoelectric disc of the buzzer model is used, with its coefficients ($d_{33}$, $\varepsilon_r$, and $\varepsilon_0$) extracted from the catalog by Shibuya (2001) and incorporated into Eq. (3). Below, the definitions of $d_{33}$ , $\varepsilon_r$ , and $\varepsilon_0$ are discussed:

$d_{33}$: In piezoelectric materials, $d_{33}$ is one of the key parameters used to describe the material's piezoelectric properties. Specifically, $d_{33}$ represents the piezoelectric charge coefficient in the direction of the applied electric field. The value of $d_{33}$ is critical for designing devices that rely on the piezoelectric effect, as it helps in understanding and predicting how the material will behave under electrical and mechanical loads. It assists engineers and scientists in selecting the right material for specific applications by indicating how efficiently a material can convert electrical energy into mechanical energy or vice versa.

$\varepsilon_0$ : $\varepsilon_0$ is the permittivity of a vacuum, which quantifies the ability of free space to permit electric field lines. It serves as a baseline or reference value for the dielectric properties of materials. It plays a crucial role in understanding how piezoelectric materials behave under electric fields. The value of $\varepsilon_0$ is approximately $8.854*10^{-12}$ farads per meter (F/m).

$\varepsilon_r$ : The relative permittivity,$\varepsilon_r$, is a dimensionless number that describes how much the material can increase the capacitance of a capacitor compared to the capacitance of the same capacitor in a vacuum. It essentially measures the material's ability to store electrical energy in the presence of an electric field. The absolute permittivity $\varepsilon$ of a material is the product of $\varepsilon_r$ and $\varepsilon_0$ (the permittivity of free space). Mathematically: $\varepsilon = \varepsilon_r \cdot \varepsilon_0$

$$V = \frac{d_{33} F t}{\varepsilon_r \varepsilon_0 A} \rightarrow P = \frac{V \varepsilon_r \varepsilon_0}{d_{33} t} \tag{3}$$

The piezoelectric used is a disc-shaped ceramic with a diameter of 27 mm, and the values related to Eq. (3) are given in Table 2. The pressures extracted using Eq. (4) are then converted to Sound Pressure Level (SPL) (Mitrović et al., 2010).

$$SPL = 20 log_{10} \frac{P_{rms}}{P_{ref}} \quad P_{ref} = 20\ \mu Pa, \quad P_{rms} = \text{root mean square of pressure} \tag{4}$$

Out of 36 series of signals extracted from the experiments, one series was examined to estimate the minimum time required for testing. For example, signals related to the test conducted at 2.5 m/s, lasting 40 minutes, and in area A1 were analyzed. After performing Fast Fourier Transform (FFT) on the mentioned test signals, the acoustic power spectrum was calculated and is presented in Fig. 23 (a). Based on Fig. 23 (b), there is no significant change in the average amplitude or pulse of the signal throughout the entire test period. The uniformity of both the maximum and minimum signal amplitudes indicates that by determining the minimum time required to induce erosion in the 3 sections of the sample plate, we

**Table 2 ceramic piezoelectric materials characteristics (Shibuya, 2001)**

| Item | Symbol (Unit) | P-7 |
|---|---|---|
| Piezoelectric Constant | $d_{33}$ $(10^{-12} m/V)$ | 410 |
| Relative Dielectric Constant | $\varepsilon_r$ | 2100 |
| Vacuum permittivity | $\varepsilon_0$ $(Farad/m)$ | $8.854*10^{-12}$ |
| Thickness | t (mm) | 0.3 |

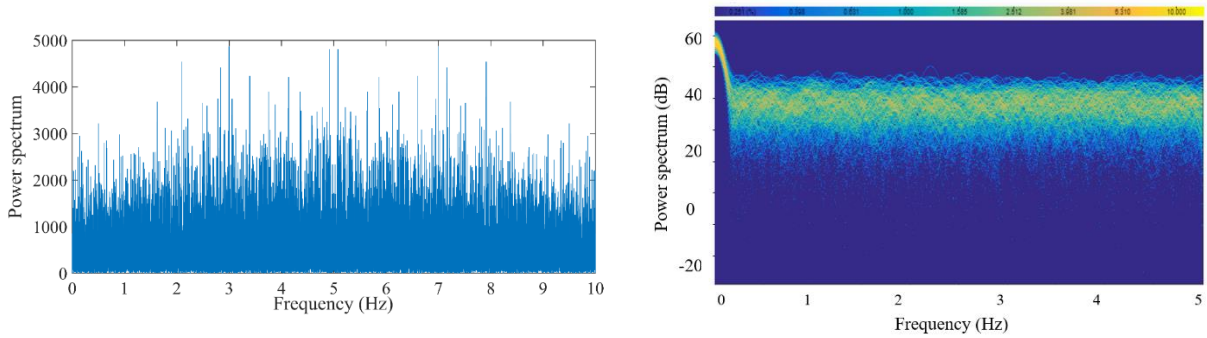


(a) (b)

**Fig. 23 Acoustic power spectrum (b): Acoustic power spectrum in Db**

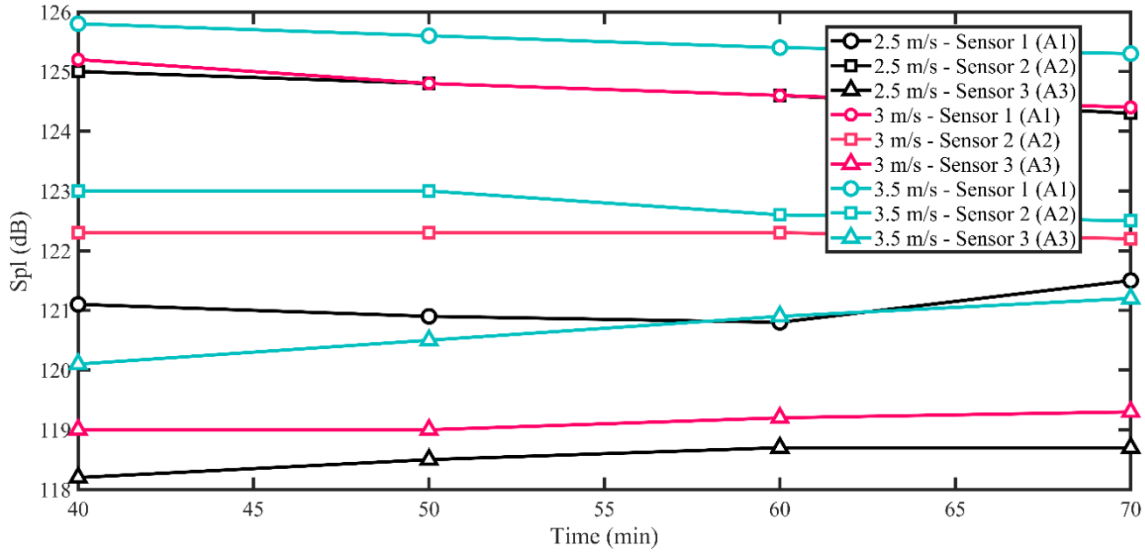


**Fig. 24 Variations in SPL with time at different velocities**

**Table 3 Percentage thresholds of eroded surface and SPL in three sections of the sample plate at different velocities over a 40-minute duration**

| Inlet velocity into the channel | Type of sensor and its corresponding section | Spl (dB) | Percentage of eroded (/.) surface threshold |
|---|---|---|---|
| 2.5 m/s | A251 (Sensor 1, A1) | 121.1 | 26 |
| | A252 (Sensor 2, A2) | 125 | 35 |
| | A253 (Sensor 3, A3) | 118.2 | 12 |
| 3 m/s | A301 (Sensor 1, A1) | 125.2 | 37 |
| | A302 (Sensor 2, A2) | 122.3 | 31 |
| | A303 (Sensor 3, A3) | 119 | 13 |
| 3.5 m/s | A351 (Sensor 1, A1) | 125.8 | 41 |
| | A352 (Sensor 2, A2) | 123 | 34 |
| | A353 (Sensor 3, A3) | 120.1 | 18 |

can establish a relationship between SPL and the achieved erosion level. This relationship can be used to properly assess the correct placement of the piezoelectric device and also formulate this relationship mathematically.

Also, in Fig. 24, changes in SPL with time at different velocities are depicted. In this plot, the variations in SPL across different sensors show minimal increases with time, reaching a maximum of approximately 0.7%. Therefore, the minimum time required to reach the erosion threshold (which is approximately 40 minutes) is considered. In this study, given that a color test is used, the erosion threshold is defined as the point at which erosion becomes visible at all tested speeds in each of the three sections of the sample plate (A1, A2, A3). This visibility allows for the evaluation of both the Sound Pressure Level (SPL) and the erosion occurring in each section of the sample plate.

Based on the provided explanation, 40 minutes are allocated for assessing the correct placement of the piezoelectric sensors. Accordingly, Table 3 presents the values of SPL (Sound Pressure Level) and the level of

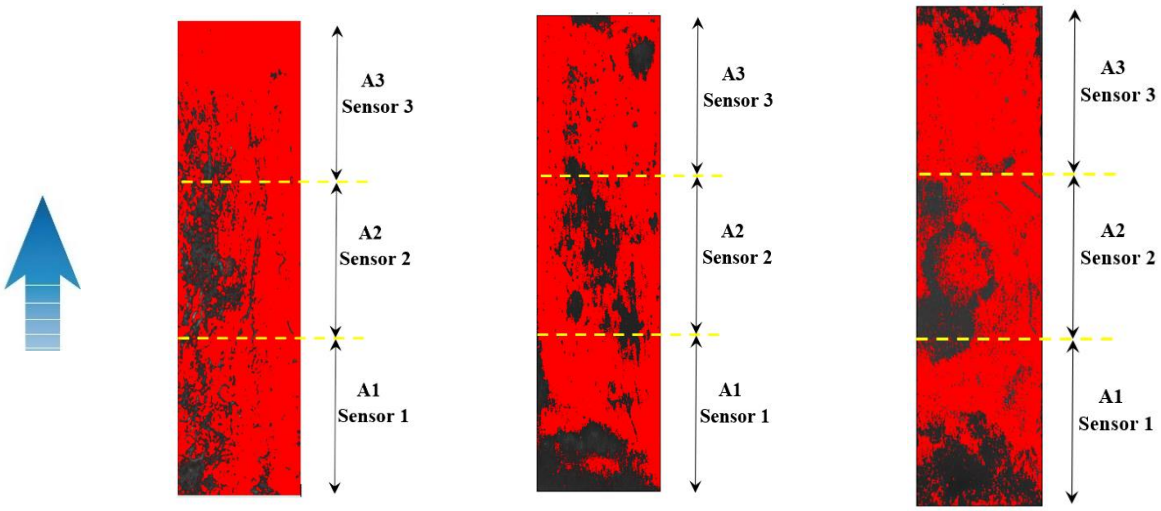


Flow direction (a): 2.5 m/s (b): 3 m/s (c): 3.5 m/s

**Fig. 25 The threshold of the erosion level at different input speeds over 40 minutes**

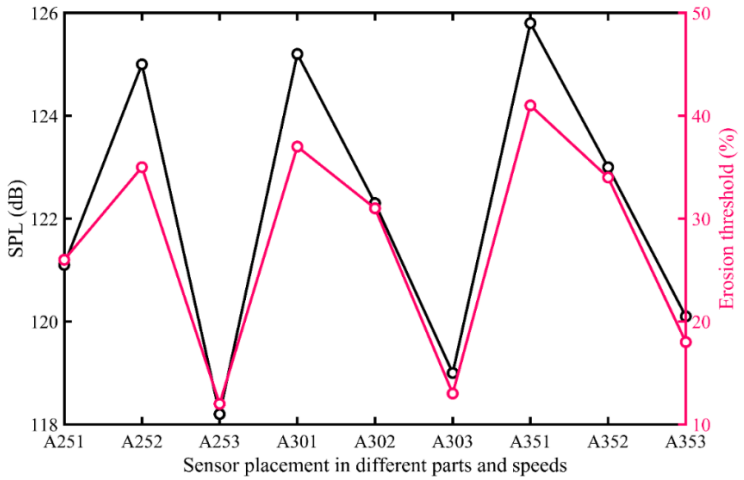


**Fig. 26 Correlation of SPL and eroded surface during 40 minutes at different speeds**

erosion observed at different velocities over the 40-minute period.

In Fig. 25, the threshold of the eroded surface is shown at various velocities, each with a 40-minute duration, for comparison with SPL. Sensor 1 is located in zone A1, Sensor 2 is located in zone A2, and Sensor 3 is located in zone A3.

Based on Table 3, when both the fluid flow rate and sensor position need to be specified simultaneously, the notation [A (speed*10) (Sensor Number)] is used. For example, if the fluid speed is 3.5 m/s and the sensor position is number 2, the notation A352 is applied. SPL values for sensors 1, 2, and 3 were measured at flow speeds of 2.5 m/s, 3 m/s, and 3.5 m/s, respectively. The percentage of the erosion threshold was also measured in zones A1, A2, and A3. The SPL values and the erosion threshold percentages are shown on the left and right sides of the graph in Fig. 26 at 40 minutes. As depicted in Fig. 26, , changing the sensor position at each speed causes the SPL value to either increase or decrease. Concurrently, the erosion threshold increases with higher SPL and decreases with lower SPL. Although the units of SPL and the erosion threshold are different and not directly comparable quantitatively, the simultaneous increase and decrease in SPL and the percentage of the eroded surface indicate the proper arrangement of measurement sensors and validate the effective placement of piezoelectrics. This result is significant and suggests that further experiments could establish a relationship between SPL and the erosion threshold.

## 4. CONCLUSION

In this study, for the first time, the correct placement and arrangement of piezoelectric sensors for capturing cavitation signals using CFD analysis have been addressed. A semi-cylindrical bluff body has been utilized as the optimal obstacle to enhance cavitation formation in the test section of the designed channel. Following various experiments in this research, it has been determined that using a Film Applicator is the best method for achieving uniform color with minimal thickness and without excessive adherence to the sample plate. Since the

piezoelectric sensors do not come into direct contact with the sample plate, they are installed where their flow pattern mimics that downstream of the primary bluff body.

The study focuses on the correct placement and arrangement of piezoelectric sensors for capturing cavitation signals. Conducted in the K23 cavitation tunnel, a converging-diverging channel was designed for this purpose, employing a semi-cylindrical bluff body to enhance cavitation inception. The piezoelectric sensors are positioned based on CFD analysis at three different distances from the three bluff bodies. Initially, the minimum time required to create wear in three sections of the sample plate was determined, establishing the relationship between SPL (Sound Pressure Level) and the resulting wear surface to investigate the proper placement of piezoelectrics. Following experiments at different velocities (entry speed into the measurement section), the correlation between cavitation-induced erosion and SPL generated at each piezoelectric sensor is examined. Point-by-point monitoring of cavitation-induced erosion and SPL illustrates simultaneous increases and decreases, validating the correct positioning of the piezoelectric sensors.

## CONFLICT OF INTEREST

The authors confirm that there are no conflicts of interest associated with the publication of this manuscript.

## REFERENCES


Bajic, B. (2002). Multidimensional Diagnostics of turbine cavitation. *Journal of Fluids Engineering*, *124*(4), 943–950. https://doi.org/10.1115/1.1511162

Brennen, C. (1995). *Cavitation and bubble dynamics*. Oxford University Press.

Shekhani, H. (2024). *COMSOL Simulation of the Direct Piezoelectric Effect*. https://www.ultrasonicadvisors.com/comsol-simulation-of-the-direct-piezoelectric-effect

Čudina, M. (2003). Detection of cavitation phenomenon in a centrifugal pump using audible sound. *Mechanical Systems and Signal Processing*, *17*(6), 1335–1347. https://doi.org/10.1006/MSSP.2002.1514

Čudina, M., & Prezelj, J. (2008). Use of audible sound for safe operation of kinetic pumps. *International Journal of Mechanical Sciences*, *50*(9), 1335–1343. https://doi.org/10.1016/J.IJMECSCI.2008.07.012

De, M. K., & Hammitt, F. G. (1982). New method for monitoring and correlating cavitation noise to erosion capability. *Journal of Fluids Engineering*, *104*(4), 434–441. https://doi.org/10.1115/1.3241876

Dunlop, R. (2015). *Simulating Two Phase Flows Using Star-CCM+*. MSc thesis, University of Glasgow, Glasgow, Scotland, UK .https://doi.org/10.13140/RG.2.2.33922.38088

Elforjani, M., & Mba, D. (2009). Detecting natural crack initiation and growth in slow speed shafts with the Acoustic Emission technology. *Engineering Failure Analysis*, *16*(7), 2121–2129. https://doi.org/10.1016/J.ENGFAILANAL.2009.02.005

Escaler, X., Avellan, F., & Egusquiza, E. (2001). *Cavitation Erosion prediction from inferred forces using material resistance data*. 4th International Symposium on Cavitation (CAV2001).

Escaler, X., Farhat, M., Avellan, F., & Egusquiza, E. (2003). Cavitation erosion tests on a 2D hydrofoil using surface-mounted obstacles. *Wear*, *254*(5–6), 441–449. https://doi.org/10.1016/S0043-1648(03)00261-8

Flageul, C., Fortes, R., & Archer, A. (2012). Cavitation erosion prediction by numerical simulations. *14th International Symposium on Transport Phenomena and Dynamics of Rotating Machinery*, Honolulu, HI, USA.

François, L. (2012). *Vibratory detection system of cavitation erosion: historic and algorithm validation*. 325–330. https://doi.org/10.3850/978-981-07-2826-7_150

Garcia, R., & Hammitt, F. G. (1966). *Cavitation damage and correlations with material and fluid properties*. http://deepblue.lib.umich.edu/handle/2027.42/5008

Ge, H., Li, J., & Chen, H. (2016). Cavitation noise from elastic response of metals in ultrasonic cavitation erosion. *Proceedings of the Institution of Mechanical Engineers, Part J: Journal of Engineering Tribology*, *230*(7). https://doi.org/10.1177/1350650115619149

Ghahramani, E., Jahangir, S., Neuhauser, M., Bourgeois, S., Poelma, C., & Bensow, R. E. (2020). Experimental and numerical study of cavitating flow around a surface mounted semi-circular cylinder. *International Journal of Multiphase Flow*, *124*, https://doi.org/10.1016/j.ijmultiphaseflow.2019.103191

Hattori, S., & Ishikura, R. (2010). Revision of cavitation erosion database and analysis of stainless steel data. *Wear*, *268*(1–2), 109–116. https://doi.org/10.1016/J.WEAR.2009.07.005

Hattori, S., Mori, H., & Okada, T. (1998). Quantitative evaluation of cavitation erosion. *Journal of Fluids Engineering*, *120*(1), 179–185. https://doi.org/10.1115/1.2819644

He, Y., & Shen, Z. (2022) *Experimental Research on Cavitation Erosion Detection Based on Acoustic Emission Technique*. www.ndt.net/EWGAE-ICAE2012/

Helal, M. M., Ahmed, T. M., Banawan, A. A., & Kotb, M. A. (2018). Numerical prediction of sheet cavitation on marine propellers using CFD simulation with transition-sensitive turbulence model. *Alexandria Engineering Journal*, *57*(4). https://doi.org/10.1016/j.aej.2018.03.008

Jahangir, S., Ghahramani, E., Neuhauser, M., Bourgeois, S., Bensow, R. E., & Poelma, C. (2021). Experimental investigation of cavitation-induced erosion around a surface-mounted bluff body. *Wear*, *480–481*. https://doi.org/10.1016/j.wear.2021.203917

Jirarungsatian, C., & Prateepasen, A. (2010). Pitting and uniform corrosion source recognition using acoustic emission parameters. *Corrosion Science*, *52*(1), 187–197. https://doi.org/10.1016/J.CORSCI.2009.09.001

Ju, H. J., & Choi, J. S. (2022). Experimental study of cavitation damage to marine propellers based on the rotational speed in the coastal waters. *Machines*, *10*(9). https://doi.org/10.3390/machines10090793

Karimi, A., & Martin, J. L. (2013). Cavitation erosion of materials. *International Metals Reviews. 1986*, *31*(1), 1-26. https://doi.org/10.1179/IMTR.1986.31.1.1

Lee, I., Park, S., Seok, W., & Rhee, S. H. (2021). A Study on the cavitation model for the cavitating flow analysis around the marine propeller. *Mathematical Problems in Engineering*, *2021*. https://doi.org/10.1155/2021/2423784

Lush, P. A., & Angell, B. (1984). Correlation of cavitation erosion and sound pressure level. *Journal of Fluids Engineering*, *106*(3), 347–351. https://doi.org/10.1115/1.3243126

Mardin, H., Kamil, K., Amri, A., & Rizal, M. (2023). *Sound absorption analysis of carbon steel varied in density and microstructures.* Inter-Noise And Noise-Con Congress and Conference Proceedings, 268(3), 5434–5439. https://doi.org/10.3397/IN_2023_0768

Mitrović, D., Zeppelzauer, M., & Breiteneder, C. (2010). *Features for content-based audio retrieval*. Advances in Computers (Vol. 78, pp. 71–150). Academic Press Inc. https://doi.org/10.1016/S0065-2458(10)78003-7

Momma, T., & Lichtarowicz, A. (1995). A study of pressures and erosion produced by collapsing cavitation. *Wear*, *186–187*(PART 2), 425–436. https://doi.org/10.1016/0043-1648(95)07144-X

Shibuya, K., (2001), Murata Manufacturing catalog. Piezoelectric Ceramic Sensors (PIEZOTITE) [Cat. No. P19E-7], Tokyo, Ceramic Society of Japan. http://www.murata.com

Nadery, A., Ghassemi, H., & Chybowski, L. (2021). The effect of the PSS configuration on the hydrodynamic performance of the KP505 propeller behind the KCS. *Ocean Engineering*, *234*, 109310. https://doi.org/10.1016/J.OCEANENG.2021.109310

Richman, R. H., & McNaughton, W. P. (1990). Correlation of cavitation erosion behavior with mechanical properties of metals. *Wear*, *140*(10), 63–82. https://doi.org/10.1016/0043-1648(90)90122-Q

Siemens Digital Industries Software. (2021). *Simcenter STAR-CCM+ Documentation Version 2021.2*. https://www.plm.automation.siemens.com/global/en/products/simcenter/STAR-CCM.html

Sikirica, A., Carija, Z., Kranjcevic, L., & Lucin, I. (2019). Grid type and turbulence model influence on propeller characteristics prediction. *Journal of Marine Science and Engineering*, *7*(10). https://doi.org/10.3390/jmse7100374

Sipilä, T. P., Sánchez-Caja, A., & Siikonen, T. L. (2014). *Eddy vorticity in cavitating tip vortices modelled by different turbulence models using the rans approach.* 11th World Congress on Computational Mechanics, WCCM 2014, 5th European Conference on Computational Mechanics, ECCM 2014 and 6th European Conference on Computational Fluid Dynamics, ECFD 2014.

Steller, J., Gireń, B. G., & Polska Akademia Nauk. (2015). *International Cavitation Erosion Test Final Report*.

Tunnel, C. (2001). *K23 cavitation tunnel*. Cussons Technology Ltd https://www.cussons.co.uk.

Varga, J. J., Sebestyen, G., & Fay, A. (1969). Detection of cavitation by acoustic and vibration-measurement methods. *La Houille Blanche*, *55*(2). https://doi.org/10.1051/lhb/1969012

Yamagata, T., Saito, N., & Fujisawa, N. (2016). Aeolian tone from a semi-circular cylinder in a stream. *Journal of Flow Control, Measurement & Visualization*, *04*(01), 30–37. https://doi.org/10.4236/jfcmv.2016.41003

Ylönen, M., Saarenrinne, P., Miettinen, J., Franc, J.-P., Fivel, M. C., Laakso, J., Esti, al, & Fivel, M. (2020). Estimation of cavitation pit distributions by acoustic emission. *Journal of Hydraulic Engineering*, *2020*(2). https://doi.org/10.1061/(ASCE)HY.1943-7900.0001686ï

Zhang, S., Qian, Z., & Ji, B. (2022). Estimation of cavitation erosion area in unsteady cavitating flows using a modified approach. *Ocean Engineering*, *262*(February 2021), 112229. https://doi.org/10.1016/j.oceaneng.2022.112229